

Learned Hemodynamic Coupling Inference in Resting-State Functional MRI

William Consagra^a, Eardi Lila^b

^a*Dept. of Statistics, University of South Carolina, 1523 Greene St, Columbia, 29225, SC, USA*

^b*Dept. of Biostatistics, University of Washington, 4333 Brooklyn Avenue NE, Seattle, 98195, WA, USA*

Abstract

Functional magnetic resonance imaging (fMRI) provides an indirect measurement of neuronal activity via hemodynamic responses that vary across brain regions and individuals. Ignoring this hemodynamic variability can bias downstream connectivity estimates. Furthermore, the hemodynamic parameters themselves may serve as important imaging biomarkers. Estimating spatially varying hemodynamics from resting-state fMRI (rsfMRI) is therefore an important but challenging blind inverse problem, since both the latent neural activity and the hemodynamic coupling are unknown. In this work, we propose a methodology for inferring hemodynamic coupling on the cortical surface from rsfMRI. Our approach avoids the highly unstable joint recovery of neural activity and hemodynamics by marginalizing out the latent neural signal and basing inference on the resulting marginal likelihood. To enable scalable, high-resolution estimation, we employ a deep neural network combined with conditional normalizing flows to accurately approximate this intractable marginal likelihood, while enforcing spatial coherence through priors defined on the cortical surface that admit sparse representations. Uncertainty in the hemodynamic estimates is quantified via a double-bootstrap procedure. The proposed approach is extensively validated using synthetic data and real fMRI datasets, demonstrating clear improvements over current methods for hemodynamic estimation and downstream connectivity analysis.

Keywords: Hemodynamic coupling, hemodynamic inversion, deep learning, fMRI.

1. Introduction

1.1. Motivation

Functional magnetic resonance imaging (fMRI) is a non-invasive imaging technique widely used to study neural activity. fMRI collects time-dependent blood oxygenation level-dependent (BOLD) signals, which reflect hemodynamic changes associated with neural activity (Ogawa et al., 1992). Accurate characterization of the hemodynamic coupling, i.e., the forward model that maps neural activity to BOLD signals, enables inference of underlying neural activity by solving the *hemodynamic inverse problem* (Buckner, 2003). However, this problem is complicated by the fact that the hemodynamic coupling is partially unknown and varies both across brain regions and between individuals (Loh et al., 2008; Bailes et al., 2023). Failure to account for the spatially varying hemodynamics can bias downstream estimates of functional connectivity (Lindquist et al., 2009; Rangaprakash

et al., 2018, 2023). Additionally, the hemodynamic properties are themselves of independent interest as potential imaging biomarkers. Indeed, systematic hemodynamic alterations have been identified in a variety of neuropsychiatric conditions, including autism (Yan et al., 2018), schizophrenia and bipolar disorder (Yan et al., 2021), and obsessive compulsive disorder (Rangaprakash et al., 2021).

There exists a substantial body of work on estimating hemodynamic coupling in task/event-based fMRI designs (Lange and Zeger, 2002; Wang et al., 2013; Zhang et al., 2012, 2013). In this setting, the neural signals are assumed to be known from the experimental design, making inversion considerably easier than in resting-state fMRI (rsfMRI), where both neural signals and hemodynamic response are unknown. The resting-state setting therefore leads to a challenging *blind inverse problem*, which is the focus of this work.

1.2. Related Work

The hemodynamic coupling is often modeled as a linear time-invariant system (LTI), in which the BOLD signal is expressed as a convolution of the underlying neural signals and the *hemodynamic response function* (HRF). In rsfMRI, many approaches avoid explicitly addressing the resulting blind inverse problem by assuming a known, spatially fixed HRF and then recover neural activity by solving the resulting (misspecified) linear inverse problem under a variety of spatio-temporal smoothness/sparsity priors (Karahanoğlu et al., 2013; Caballero-Gaudes et al., 2019; Uruñuela et al., 2024). In contrast, methods accommodating unknown hemodynamic couplings are less common: Cherkaoui et al. (2021) use a template-shifted HRF and combine atlas-based low-rank and total-variation penalties for estimation; Wu et al. (2013) use a two-stage procedure that first thresholds to detect activation and then estimates the HRF; Singh et al. (2020) use a reparameterization approach based on the Wiener deconvolution and estimate the HRF using nonlinear least squares.

A separate line of work uses nonlinear state-space models for coupling latent neural dynamics with more general, biophysically interpretable hemodynamic forward models (Buxton et al., 1998), with inference procedures adapted to resting-state designs (Havlicek et al., 2011). However, due to heavy computational costs, such approaches are generally limited to modeling a small number of brain regions (Cao et al., 2019), effectively imposing a strong limitation on spatial resolution. Moreover, for many practical acquisition protocols, several of the hemodynamic parameters in such models have questionable statistical identifiability (Zayane and Laleg-Kirati, 2015).

There is an extensive body of work addressing the closely related problem of blind image deblurring, where the goal is to recover both an unknown sharp image and the corresponding blur kernel from a noisy, blurred observation. Most approaches estimate image and kernel jointly, via alternating optimization (Chan and Wong, 1998) or deep learning based approaches (Gossard and Weiss, 2024). In contrast, Wipf and Zhang (2014) outlines that, while the joint reconstruction problem is often severely ill-posed, the task can be decomposed into two more manageable subproblems: first marginalizing the image out of the data likelihood and estimating the blur by maximizing the resulting marginal likelihood, and then performing non-blind deblurring given the estimated kernel. While related, this class of blind image deblurring problems is structurally different from the blind hemodynamic inverse problem, as the former typically involves only a single unknown

image-kernel pair, whereas the latter involves many coupled blind problems with complex underlying spatial dependencies in both signals and hemodynamics.

1.3. Our Contribution

In this work, we propose a novel methodology for estimating hemodynamic coupling in rsfMRI. In the spirit of Wipf and Zhang (2014), our estimator is based on a learned approximation to the marginal likelihood with respect to the latent neural signals, which enables us to decouple estimation of the forward hemodynamic coupling model from reconstruction of neural activity. The marginal likelihood is efficiently approximated using a conditional neural spline normalizing flow, trained using a biologically motivated neural-hemodynamic simulator model. This model is calibrated to real fMRI signals using a spectral moment-matching approach that guarantees the generative process produces physiologically plausible signals. Spatial regularization based on a latent Gaussian process prior is used to promote locally similar hemodynamic couplings across the cortical surface. We propose an estimation algorithm that leverages automatic differentiation of the learned likelihood and the sparsity structure of the Gaussian process prior to enable computational scalability to ultra high-resolution surface meshes. Uncertainty in the hemodynamic estimates is quantified via a double-bootstrap procedure, and automatic procedures for the selection of all model hyperparameters are proposed. Estimating the hemodynamic coupling enables the use of off-the-shelf methods to recover neural signals from BOLD data. Through extensive experiments using both synthetic and real data, we demonstrate substantial improvements over competing approaches in both hemodynamic estimation and downstream functional connectivity analysis.

2. Models and Background

This section outlines the models used for simulating neural activity and observed hemodynamic signals. Specifically, Section 2.1 introduces the neural activity model, Section 2.2 describes the signal-induced hemodynamic response model, and Section 2.3 proposes a statistical model for the observed rsfMRI data. Figure 1 illustrates the generative process. Notably, the inversion method in Section 3 is largely simulator-agnostic, so alternative neural signal, hemodynamic, or noise models can be accommodated with minor modifications. Throughout, we will assume the fMRI time series are sampled at a constant repetition time $t_r > 0$, with accompanying acquisition times $t_m = (m - 1)t_r$, for $m = 1, \dots, M$, spanning the interval $[0, (M - 1)t_r]$.

2.1. Modeling Neural Population Dynamics

Denote the brain cortical surface by $\Omega \subset \mathbb{R}^3$. At location $x \in \Omega$, we model the time-dependent neural activity, denoted by $s(x, t)$, as a sum of scaled and shifted Dirac delta functions of the form

$$s(x, t) = \sum_{i=1}^{n_x} a_{x,i} \delta(t - t_{x,i}). \quad (1)$$

We assume that the number of spikes n_x and their occurrence times $t_{x,1}, \dots, t_{x,n_x}$ are generated by a homogeneous Poisson process on $[0, (M - 1)t_r]$ with rate λ_x . The spike amplitude

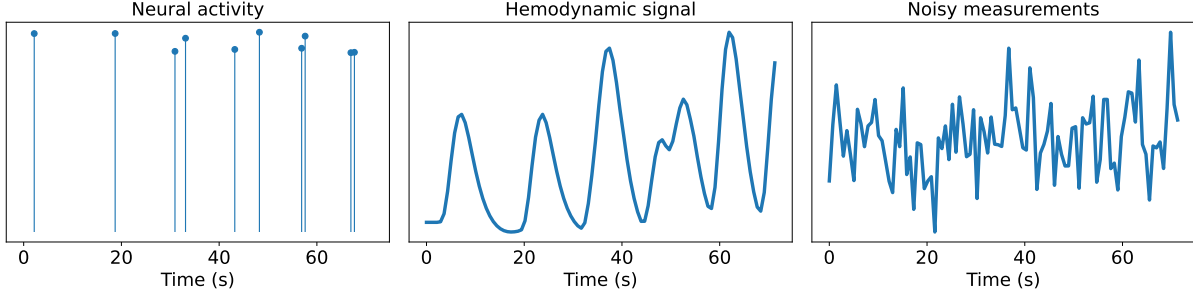


Figure 1: Simulation from the data generative model. (Left) Neural activity sampled from (2). (Middle) Hemodynamic response obtained by convolving the neural activity with the HRF (20) under forward model (3). (Right) Simulated BOLD measurements generated according to (4) ($t_r = 0.72$ s).

parameters $\{a_{x,i}\}_{i=1}^{n_x}$ are assumed to be independent and identically distributed uniform random variables on the interval (a_{\min}, a_{\max}) . Given the local heterogeneity in grey-matter tissue composition, along with the complex network of non-local white-matter structural connections, the rate λ_x is expected to vary across Ω . To capture the marginal effect of this variability, we assume λ_x is a random uniform variable on the interval $(\lambda_{\min}, \lambda_{\max})$. Putting this all together, we have the following hierarchical model for neural activity at $x \in \Omega$:

$$\begin{aligned}
 \lambda_x &\sim \text{Unif}([\lambda_{\min}, \lambda_{\max}]) \\
 (t_{x,1}, t_{x,2}, \dots, t_{x,n_x}) &\sim \text{HPP}(\lambda_x t_r (M - 1)) \\
 a_{x,i} &\sim \text{Unif}([a_{\min}, a_{\max}]), \quad i = 1, \dots, n_x \\
 s(x, t) &= \sum_{i=1}^{n_x} a_{x,i} \delta(t - t_{x,i})
 \end{aligned} \tag{2}$$

2.2. Modeling the Hemodynamic Response

Changes in local neural activity induce changes in cerebral blood flow. We model this *hemodynamic coupling* using an operator $\mathcal{H}_\theta : L^2(\mathbb{R}) \mapsto \mathcal{C}(\mathbb{R})$, parameterized by $\theta \in \Theta \subset \mathbb{R}^J$. Due to tissue heterogeneity, the hemodynamic coupling can vary across Ω . We accommodate this variability by modeling the hemodynamic parameters θ as a J -dimensional field on the cortical surface, $\theta : \Omega \mapsto \Theta$. Therefore, at $x \in \Omega$, the hemodynamic response $\mathcal{H}_{\theta(x)}$ is fully characterized by the J -dimensional parameter $\theta(x)$.

In this work, we will consider LTI forward models of the form

$$\mathcal{H}_{\theta(x)}[s(x, \cdot)](t) = \int_0^t h_{\theta(x)}(t - u) s(x, u) du, \tag{3}$$

where $h_{\theta(x)}$ is a parametric kernel. The hemodynamic parameters are often constrained componentwise to ensure biophysically plausible behavior, so we assume that the parameter space is $\Theta = \{\theta \in \mathbb{R}^J : \theta_{j,\min} \leq \theta_j \leq \theta_{j,\max}\}$. While specifying a reasonable prior model for the dependence structure of θ over Ω is challenging, we can nevertheless simulate marginal hemodynamics at $x \in \Omega$ by adopting a non-informative box-uniform prior over the parameter space, $\theta(x) \sim \text{Unif}(\Theta)$.

For estimation, it will be useful to map the constraints on Θ to an unconstrained space. To do so, we define the modified probit link function $g(\theta) = (g_1(\theta_1), \dots, g_J(\theta_J))$ by

$$\tilde{\theta}_j := g_j(\theta_j) = \Phi^{-1} \left(\frac{\theta_j - \theta_{j,\min}}{\theta_{j,\max} - \theta_{j,\min}} \right), \quad j = 1, \dots, J$$

where Φ^{-1} denotes the inverse cdf of the standard normal distribution. We denote the transformed parameters $\tilde{\theta} = g(\theta)$ and transformed parameter space by $\tilde{\Theta} = \{\tilde{\theta} = g(\theta) : \theta \in \Theta\}$.

2.3. Statistical Model for Observed Data

For a set of cortical locations $\mathcal{X} := \{x_1, \dots, x_V\} \subset \Omega$, we gather noisy observations of the induced hemodynamic response at each of the acquisition times t_1, \dots, t_M . The noise process contaminating the signals includes physiological and scanner contributions that may induce temporal autocorrelation (Lindquist, 2008). For sufficiently small t_r , this autocorrelation can be modeled and removed during preprocessing, yielding an approximately white error process, which we assume here. The resulting Gaussian measurement noise model for the observed fMRI signals is then given by

$$y_{v,m} = \mathcal{H}_{\theta(x_v)}[s(x_v, \cdot)](t_m) + \epsilon(x_v, t_m), \quad (4)$$

for $v = 1, \dots, V$; $m = 1, \dots, M$, with ϵ a stationary zero mean white noise process with $\text{Cov}(\epsilon(x, t), \epsilon(x', t')) = \sigma^2 \mathbb{I}\{x = x', t = t'\}$.

3. Methodology

As outlined in Section 1, direct joint estimation of the neural signals and hemodynamic parameters is often severely ill-posed and can lead to unstable inference. We instead marginalize over the neural signal generative process and base hemodynamic coupling estimation on the resulting (learned) marginal likelihood. To share information across space, we impose a Gaussian process prior on the hemodynamic parameter field and derive an estimator that is scalable to high-resolution cortical surface meshes. We then describe procedures for model hyperparameter selection and for quantifying estimation uncertainty. Finally, given the stage-one hemodynamic estimate, neural signal recovery reduces to a more stable non-blind inverse problem.

We denote the data matrix $Y \in \mathbb{R}^{V \times M}$, where the v -th row is the vector $y_v = (y_{v,1}, \dots, y_{v,M})$, with $y_{v,m}$ defined by Equation (4). With slight abuse notation, define $\theta, \tilde{\theta} \in \mathbb{R}^{V \times J}$ to be the hemodynamic parameter field, and its transformation under g , discretized over \mathcal{X} ; i.e., $\theta_{v,j} = \theta_j(x_v)$ and $\tilde{\theta}_{v,j} = (g(\theta))_{v,j}$, respectively. Finally, define $\text{vec} : \mathbb{R}^{n \times m} \mapsto \mathbb{R}^{nm}$ as the vectorization operator which stacks columnwise.

3.1. Learned Marginal Likelihood

We define the marginal likelihood at location $x_v \in \mathcal{X}$, in terms of the unconstrained parameters $\tilde{\theta} = g(\theta)$, as

$$p(y_v | \tilde{\theta}(x_v)) = \int_{\mathcal{S}} p(y_v | s, \tilde{\theta}, x_v) p(s | x_v) ds, \quad (5)$$

where the likelihood $p(y_v|s, \tilde{\theta}, x_v)$ is defined by (4), the point-wise signal prior $p(s|x_v)$ is defined by (2), and \mathcal{S} denotes the space of signals spanned by the generative model. For tractability, we ignore the complex spatial dependence among neural signals and instead we approximate the joint prior over \mathcal{X} by a product of the marginal priors outlined in Section 2.1. It follows that $p(Y|\theta, \mathcal{X}) \approx \prod_{v=1}^V p(y_v|\tilde{\theta}(x_v))$, hence it suffices to focus on the location-specific model in (5). Two major challenges arise. First, the marginalization integral in (5) does not admit a closed-form solution. Although a Monte Carlo approximation can be obtained by repeatedly simulating from (1) and (4), this is computationally prohibitive for large V , so a more scalable approximation is required. Second, $p(y_v|\tilde{\theta}(x_v))$ is typically high-dimensional, making it challenging to estimate. The remainder of this section outlines our approach to addressing these issues. For notational simplicity, we henceforth suppress the explicit dependence of (5) on x .

To handle the high-dimensionality of the observed signals y , we propose performing dimension reduction by learning a summary statistic $T : \mathbb{R}^M \mapsto \mathbb{R}^D$, where $D \ll M$, and basing inference off $p(T(y)|\tilde{\theta}) \approx p(y|\tilde{\theta})$. While the approximation becomes an equality if T is sufficient, in practice, outside of special cases such as exponential families, identifying a sufficient statistic is challenging, and there is no guarantee that $D \ll M$. Instead, we look for a T that balances approximation fidelity to $p(y|\tilde{\theta})$ with sufficient dimensional reduction, i.e., providing D small enough for tractable conditional density approximation. While a variety of candidates for such a T exist, in this work we adopt the simple approach of Jiang et al. (2017), which targets the posterior mean

$$T(y) = \mathbb{E}_{p(\tilde{\theta}|y)} [\tilde{\theta}]. \quad (6)$$

The posterior mean has several attractive properties for serving as a summary statistic in our setting: i) it imposes that $D = J$, where J is the dimension of $\tilde{\theta}$, ensuring significant dimension reduction, and ii) it can be estimated using standard l_2 risk minimization.

Let $T_\psi : \mathbb{R}^M \mapsto \mathbb{R}^J$ be a flexible model depending on parameters ψ , and let $p_\gamma(\cdot|\cdot) : \mathbb{R}^J \mapsto \mathbb{R}^J$ be a flexible conditional density estimator depending on parameters γ . We approximate the target density $p(T(y)|\tilde{\theta})$ in two stages. We first learn the summary statistics by minimizing the empirical expectation

$$\hat{\psi}_N = \min_{\psi} \frac{1}{N} \sum_{i=1}^N \left\| T_\psi(y_i) - \tilde{\theta}_i \right\|_2^2, \quad (y_i, \tilde{\theta}_i) \sim p(\tilde{\theta}, y). \quad (7)$$

Next, fixing $T_{\hat{\psi}_N}$, we learn an approximation to the target marginal likelihood by maximizing the log-density

$$\hat{\gamma}_N = \max_{\gamma} \frac{1}{N} \sum_{i=1}^N \log p_\gamma(T_{\hat{\psi}_N}(y_i)|\tilde{\theta}_i) \quad (y_i, \tilde{\theta}_i) \sim p(\tilde{\theta}, y). \quad (8)$$

The training pairs $(y_i, \tilde{\theta}_i)$ from the marginal joint density $p(y, \tilde{\theta}) = p(y|\tilde{\theta})p(\tilde{\theta})$ needed to form (7) and (8) can be obtained from the simulation model outlined in Section 2.

In practice, we parameterize T_ψ as a deep multilayer perceptron (MLP) with ReLU activations and p_γ as a multilayer normalizing flow. More details on the network architecture and training can be found in Section 4.3.

3.2. Prior Distribution

Due to the spatial organization of cortical vasculature, hemodynamic parameters θ , or equivalently $\tilde{\theta}$, are expected to vary smoothly across the cortex. Accordingly, we place a multivariate mean-zero Gaussian process prior on the transformed field, $\tilde{\theta} \sim GP(0, \mathcal{C}_{\tilde{\theta}})$, where the covariance operator is assumed to be diagonal $\mathcal{C}_{\tilde{\theta}} = \bigoplus_{j=1}^J \mathcal{C}_j$. That is, the j -th component of $\tilde{\theta}$ is modeled as an independent mean-zero GP with covariance operator \mathcal{C}_j . The remainder of this section details the model for the j -th component, thereby determining the full process.

On Euclidean domains, the Matérn processes are a popular choice for modeling spatial fields due to their flexibility and the closed-form of their covariance kernel. Following Lindgren et al. (2011), such processes can be generalized to spatial signals located on the highly non-linear cortical surface Ω as the weak solutions to the following stochastic partial differential equation

$$(-\Delta_{\Omega} + \kappa_j^2 I)^{\beta_j/2} \tilde{\theta}_j(x) = \frac{1}{\tau_j} u(x), \quad x \in \Omega \quad (9)$$

with Δ_{Ω} the Laplace-Beltrami operator on Ω and u a white-noise process on Ω , along with hyper-parameters $\beta_j > 0$ dictating the smoothness, $\kappa_j > 0$ the inverse bandwidth, and the marginal variance $\eta_j = \frac{\Gamma(\beta_j-1)}{\Gamma(\beta_j)4\pi\kappa_j^{2(\beta_j-1)}\tau_j^2}$ for $\tau_j > 0$. Here, we fix $\beta_j = 2$ for all j , as is commonly done.

Assume the locations x_1, \dots, x_V coincide with the vertices of the triangulated cortical surface Ω , as is common in surface-based representation of fMRI. Using the linear finite element basis $\{\phi_v\}_{v=1}^V$ induced by this triangulation (Lai and Schumaker, 2007), define the inner product matrices with element-wise definitions

$$C_{ij} = \int_{\Omega} \phi_i \phi_j \quad G_{ij} = \int_{\Omega} [\nabla_{\Omega} \phi_i]^{\top} \nabla_{\Omega} \phi_j.$$

Then it can be shown that the weak solution to (9) under this basis implies that the discretized field $\tilde{\theta}_j = (\tilde{\theta}_j(x_1), \dots, \tilde{\theta}_j(x_V))^{\top}$ is normally distributed with precision matrix

$$Q_j = \tau_j^2 (\kappa_j^2 C + G)^{\top} C^{-1} (\kappa_j^2 C + G).$$

In practice, we use the so-called mass-lumping technique and approximate C with a diagonal matrix. This diagonal approximation ensures that Q_j is a sparse matrix. Together with the assumed independence across components, we have that $\text{vec}(\tilde{\theta}^{\top}) \sim \mathcal{N}(0, Q^{-1})$, where $Q = \text{BlockDiag}(Q_1, \dots, Q_J)$.

3.3. Point Estimation

We estimate the hemodynamic parameters of the model outlined in Section 2 by maximum a posteriori (MAP) estimation, combining the learned marginal likelihood from Section 3.1 with the spatial prior from Section 3.2. Specifically, we aim to maximize the approximate posterior density

$$p(\tilde{\theta}|Y) \approx p(\tilde{\theta}|T(y_1), \dots, T(y_V)) \propto \left[\prod_{v=1}^V p_{\tilde{\gamma}}(T_{\hat{\psi}}(y_v)|\tilde{\theta}_v) \right] p(\tilde{\theta}_1, \dots, \tilde{\theta}_V), \quad (10)$$

where $p(\tilde{\theta}_1, \dots, \tilde{\theta}_V)$ denotes the spatial prior. We leverage automatic-differentiation of the learned marginal likelihood and the sparsity structure induced by the spatial prior to compute the MAP estimates efficiently.

Specifically, we compute an approximate MAP estimate using Newton's method applied to the negative log-posterior

$$-\log p(\tilde{\theta}|Y) \propto - \sum_{v=1}^V \log p_{\tilde{\gamma}}(T_{\hat{\psi}}(y_v) | \tilde{\theta}_v) + \frac{1}{2} \text{vec}(\tilde{\theta})^\top Q \text{vec}(\tilde{\theta}). \quad (11)$$

Newton's method forms a sequence of iterates $k = 0, 1, \dots$ defined by

$$\text{vec}(\tilde{\theta}^{(k+1)}) = \text{vec}(\tilde{\theta}^{(k)}) - \alpha_k \delta^{(k)}, \quad (12)$$

where the update direction $\delta^{(k)}$ solves the linear system

$$H(\text{vec}(\tilde{\theta}^{(k)})) \delta^{(k)} = G(\text{vec}(\tilde{\theta}^{(k)})), \quad (13)$$

with $G(\text{vec}(\tilde{\theta})) \in \mathbb{R}^{VJ}$ and $H(\text{vec}(\tilde{\theta})) \in \mathbb{R}^{VJ \times VJ}$ denoting the gradient and Hessian of (11), respectively, and α_k the step-size. Although the dimensionality VJ can be very large, the linear system in (13) is tractable due to its sparsity. Specifically, notice that the gradient has the form

$$G(\text{vec}(\tilde{\theta})) = - \begin{pmatrix} \frac{\partial}{\partial \tilde{\theta}_{11}} \log p_{\tilde{\gamma}}(T_{\hat{\psi}}(y_1) | \tilde{\theta}_1) \\ \frac{\partial}{\partial \tilde{\theta}_{21}} \log p_{\tilde{\gamma}}(T_{\hat{\psi}}(y_2) | \tilde{\theta}_2) \\ \vdots \\ \frac{\partial}{\partial \tilde{\theta}_{VJ}} \log p_{\tilde{\gamma}}(T_{\hat{\psi}}(y_V) | \tilde{\theta}_V) \end{pmatrix} + Q \text{vec}(\tilde{\theta}), \quad (14)$$

and the Hessian decomposes as

$$H(\text{vec}(\tilde{\theta})) = -\nabla_{\text{vec}(\tilde{\theta})}^2 \log \prod_{v=1}^V p_{\tilde{\gamma}}(T_{\hat{\psi}}(y_v) | \tilde{\theta}_v) + Q, \quad (15)$$

with

$$\left[-\nabla_{\text{vec}(\tilde{\theta})}^2 \log \prod_{v=1}^V p_{\tilde{\gamma}}(T_{\hat{\psi}}(y_v) | \tilde{\theta}_v) \right]_{ii'} = \begin{cases} -\frac{\partial^2}{\partial \tilde{\theta}_{vj} \partial \tilde{\theta}_{vj'}} \log p_{\tilde{\gamma}}(T_{\hat{\psi}}(y_v) | \tilde{\theta}_v), & i, i' \in \mathcal{I}(v, j, j') \\ 0, & \text{otherwise.} \end{cases} \quad (16)$$

Here, \mathcal{I} is defined as

$$\begin{aligned} \mathcal{I}(v, j, j') &= \{(i, i') \text{ such that } i = (j-1)V + v; \\ & \quad i' = (j'-1)V + v; j, j' \in \{1, \dots, J\}; 1 \leq v \leq V\}. \end{aligned}$$

Notice that the element-wise definition (16) implies $\nabla_{\text{vec}(\tilde{\theta})}^2 \log \prod_{v=1}^V p_{\tilde{\gamma}}(T_{\hat{\psi}}(y_v) | \tilde{\theta}_v)$ has only J^2V non-zero terms. Given that the matrices Q_{κ_j, τ_j} are sparse, it follows that the Hessian (15) is the sum of two sparse matrices and is therefore sparse. Moreover, both (14) and (15)

depend on partial derivatives of the learned marginal likelihood, which can be computed efficiently via back-propagation. Therefore, the linear system (13) can be solved efficiently using (preconditioned) conjugate gradient type algorithms.

Given that the summary network $T_{\hat{\psi}}(\cdot)$ targets the point-wise posterior mean (6), we use the estimates $(T_{\hat{\psi}}(y_v))_v$ to form the initialization $\text{vec}(\tilde{\boldsymbol{\theta}}^{(0)})$. The step-sizes α_k are updated at each iteration by performing an Armijo line search (Armijo, 1966).

3.4. Hyperparameter Selection

3.4.1. Calibration of Smoothness Prior

The spatial prior precision matrices $(Q_j)_j$ depend on unknown hyperparameters κ_j and τ_j , controlling the bandwidth and marginal variance, respectively. To select these hyperparameters, we maximize a Laplace approximation to the log marginal likelihood $p(Y|\{\kappa_j, \tau_j\}_j)$ around the MAP estimate, which has the following well known analytic form

$$\begin{aligned} \log p(Y|\{\kappa_j, \tau_j\}_j) &\approx \sum_{v=1}^V \log p_{\hat{\gamma}}(T_{\hat{\psi}}(y_v)|\hat{\boldsymbol{\theta}}_v) - \frac{1}{2} \text{vec}(\hat{\boldsymbol{\theta}})^\top Q \text{vec}(\hat{\boldsymbol{\theta}}) \\ &+ \frac{1}{2} \log \det |Q| - \frac{1}{2} \log \det |H(\text{vec}(\hat{\boldsymbol{\theta}}))|, \end{aligned} \quad (17)$$

where $\text{vec}(\hat{\boldsymbol{\theta}})$ is the MAP estimator formed in Section 3.3 and $H(\text{vec}(\hat{\boldsymbol{\theta}}))$ is (15) evaluated at the MAP, which depends on the hyperparameters of interest $\{\kappa_j, \tau_j\}_j$ through Q .

In the absence of additional prior information, we assume $\kappa_j = \kappa$ and $\tau_j = \tau$, for all j , to reduce the dimension of the hyperparameter search. Within this reduced space, we perform a grid search, selecting κ, τ that maximize (17) over a discrete set of locations.

3.4.2. Calibration of Simulator

While $\theta_{j,\min}, \theta_{j,\max}$ are assumed known a-priori, the models in Section 2 depend on several unknown simulator hyperparameters $\nu := (\lambda_{\min}, \lambda_{\max}, a_{\min}, a_{\max}, \sigma^2)$. To calibrate ν to our observed fMRI signals, we take a spectral moment-matching based approach. Specifically, let $p(\theta, s, \epsilon|\nu)$ denote the joint distribution induced by the simulator given ν , and let $p^*(y)$ denote the true marginal distribution of the observed fMRI signals. We propose the following spectral moment-based loss for calibration

$$l_s(\nu) = \sum_{\omega \in \mathcal{W}} \left| \mathbb{E}_{p^*(y)} \left[\mathcal{P}_y(\omega) \right] - \mathbb{E}_{p(s, \theta, \epsilon|\nu)} \left[\mathcal{P}_{\mathcal{H}_\theta[s](t) + \epsilon(t)}(\omega) \right] \right|, \quad (18)$$

where \mathcal{P}_r denotes the power spectral density of the random signal r and $\mathcal{W} = \{\omega : \omega = \frac{k}{Mt_r}; k \in \{-\frac{M}{2}, \dots, \frac{M}{2}\}\}$ denotes the set of Nyquist frequencies. We use the power spectral density moments, as opposed to the raw moments, to ensure the loss is translation-invariant.

In practice, none of the quantities in (18) are available analytically. However, we can easily form an approximation via simulations, where $\mathbb{E}_{p^*(y)}$ is approximated using the observed BOLD signals and $\mathbb{E}_{p(s, \theta, \epsilon|\nu)}$ is approximated using forward model simulations. This results in the empirical loss function

$$l_s(\nu) \approx \sum_{\omega \in \mathcal{W}} \left| \frac{1}{V} \sum_{v=1}^V \left[\mathcal{P}_{y_v}(\omega) \right] - \frac{1}{K} \sum_{k=1}^K \left[\mathcal{P}_{\mathcal{H}_{\theta_k}[s_k](t) + \epsilon_k(t)}(\omega) \right] \right|, \quad (19)$$

where $(\theta_k, s_k, \epsilon_k) \sim p(\theta, s, \epsilon|\nu)$, for $k = 1, \dots, K$. Clearly, (19) is not differentiable in ν , so we use a zero-th order optimizer to estimate the minimizer (Frazier, 2018).

3.5. Uncertainty Quantification

Let $\hat{\boldsymbol{\theta}}$ denote the minimizer of (11), and define $\hat{\boldsymbol{\theta}} = g^{-1}(\hat{\boldsymbol{\theta}})$. Although not the primary focus of this work, our goal is to provide a tool to quantify the uncertainty of this estimate at a prespecified location x_v , that is, to construct intervals for $\theta_j(x_v)$.

Under the proposed Bayesian formulation, the full posterior (10) provides a natural approach to uncertainty quantification. However, its high-dimensionality and non-convexity make MCMC-based approaches to sampling (10) computationally challenging. Moreover, the resulting credibility intervals would not necessarily be well calibrated in the frequentist sense. Perhaps unsurprisingly, we found common approximations, such as the Laplace approximation, to substantially underestimate uncertainty.

We therefore propose a double bootstrap based approach, adapting the method from Hall and Horowitz (2013), originally developed for nonparametric regression, to our current setting. The algorithm is outlined below.

1. Generate B resamplings of the observed signals $Y^{(b)}$, $b = 1, \dots, B$ using the stationary bootstrap (Politis and Romano, 1994). Unlike the classical bootstrap for independent data, this method resamples temporally contiguous blocks of observations to approximately preserve the time dependence structure of the signals.
2. For each bootstrapped sample $b = 1, \dots, B$
 - (a) Estimate $\hat{\boldsymbol{\theta}}^{(b)}$ by minimizing (11) conditioned on $Y^{(b)}$
 - (b) For $r = 1, \dots, R$, generate inner block-bootstrap resamples $Y^{(b,r)}$ from $Y^{(b)}$ using the stationary bootstrap. For each inner resample, estimate $\hat{\boldsymbol{\theta}}^{(b,r)}$ by minimizing (11) conditioned on $Y^{(b,r)}$.
3. For each j , calculate the marginal variance at location x_v , $s_{\hat{\theta}_{vj}}^2$, from the outer bootstrap estimates $\{\hat{\boldsymbol{\theta}}_v^{(b)}\}_{b=1}^B$, and the variance $s_{\hat{\theta}_{vj}}^2$ from the inner bootstrap estimates $\{\hat{\boldsymbol{\theta}}_v^{(b,r)}\}_{r=1}^R$.
4. For each j , estimate the empirical coverage at location x_v using the bootstrap coverage

$$\pi_B^{(j)}(x_v, \alpha) = \frac{1}{B} \sum_{b=1}^B \mathbb{I} \left\{ \hat{\boldsymbol{\theta}}_{vj} \in \left(\hat{\boldsymbol{\theta}}_{vj}^{(b)} - z_{1-\frac{\alpha}{2}} s_{\hat{\theta}_{vj}}^{(b)}, \hat{\boldsymbol{\theta}}_{vj}^{(b)} + z_{1-\frac{\alpha}{2}} s_{\hat{\theta}_{vj}}^{(b)} \right) \right\}$$

5. For target coverage α_0 , determine $\hat{\alpha}^{(j)}(x_v, \alpha_0)$ such that $\pi_B^{(j)}(x_v, \alpha) \approx 1 - \alpha_0$. In practice, this is achieved by computing $\pi_B^{(j)}(x_v, \alpha)$ on a dense grid of candidate α 's. We then define $\hat{\alpha}_\xi^{(j)}(\alpha_0)$ to be the ξ -level quantile of $\{\hat{\alpha}^{(j)}(x_v, \alpha_0) : x_v \in \mathcal{X}\}$. In practice, we set $\xi = 0.05$.

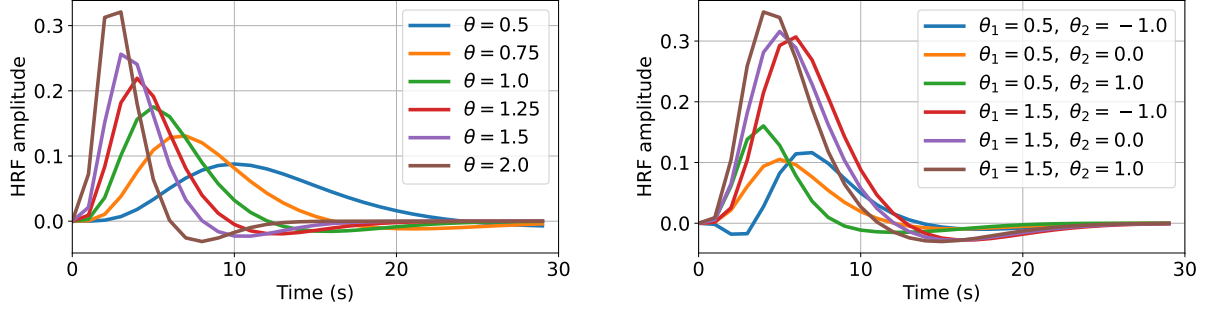


Figure 2: Hemodynamic response kernel for several θ for model (20) (left panel) and (21) (right panel).

6. Return the transformed bootstrap calibrated pointwise intervals

$$\left\{ \left(g_j^{-1} \left(\hat{\theta}_{vj} - z_{1 - \frac{\hat{\alpha}_\xi^{(j)}(\alpha_0)}{2}} s_{\hat{\theta}_{vj}} \right), g_j^{-1} \left(\hat{\theta}_{vj} + z_{1 - \frac{\hat{\alpha}_\xi^{(j)}(\alpha_0)}{2}} s_{\hat{\theta}_{vj}} \right) \right) : x_v \in \mathcal{X} \right\}.$$

4. Experiments and Implementation

4.1. Hemodynamic Models

To model the hemodynamic response, we assume an LTI forward model of the form (3) under two popular parametric kernels built from the so-called canonical double Gamma function, defined as

$$h(t) = \frac{t^{a_1-1} b_1^{a_1} \exp(-b_1 t)}{\Gamma(a_1)} - c \frac{t^{a_2-1} b_2^{a_2} \exp(-b_2 t)}{\Gamma(a_2)}$$

with constants $a_1 = 6$, $a_2 = 16$, $b_1 = 1$, $b_2 = 1$, $c = 1/6$. The first model is a one-parameter shifted double gamma model (Cherkaoui et al., 2021), given by

$$h_\theta(t) = \frac{\theta^{a_1+1} t^{a_1} \exp(-\theta t)}{\Gamma(a_1 + 1)} - c \frac{\theta^{a_2+1} t^{a_2} \exp(-\theta t)}{\Gamma(a_2 + 1)}, \quad (20)$$

with parameter bounds $\theta \in [0.5, 2.5]$. The second model is a two-parameter basis expansion of the form

$$h_\theta(t) = \theta_1 h(t) + \theta_2 \frac{\partial}{\partial t} h(t), \quad (21)$$

for which reasonable physiological ranges are $\theta_1 \in [0.2, 2.0]$, $\theta_2 \in [-1.0, 1.0]$ (Lindquist et al., 2009). Figure 2 shows how the kernel shape changes with respect to θ for both models.

4.2. Datasets

4.2.1. In-vivo Data

We use data from the publicly available Young Adult Human Connectome Project (HCP-YA) (Glasser et al., 2016) to evaluate our method. Specifically, we use the preprocessed rsfMRI data, denoised with ICA-FIX (Salimi-Khorshidi et al., 2014), and mapped to the left cortical surface mesh with 32,492 vertices and registered using FreeSurfer. Details on the acquisition and preprocessing protocols can be found in the standard reference (Glasser et al., 2013), and are thus omitted here.

4.2.2. Synthetic Data

A synthetic hemodynamic parameter field $\tilde{\theta}$ is sampled from the GP prior outlined in Section 3.2, with $\kappa = 5 \cdot 10^{-3}$, $\tau^2 = 10^4$ for the 1-parameter model (20) and $\kappa_1 = \kappa_2 = 5 \cdot 10^{-2}$, $\tau_1^2 = \tau_2^2 = 10^4$ for the 2-parameter model (21). The calibration procedure from Section 3.4.2 was run on the rsfMRI data of a randomly selected HCP-YA subject under both hemodynamic forward models, and the results were used to parameterize the neural signal simulator (Section 2.1) and measurement error model (Section 2.3). Using the calibrated simulator and hemodynamic parameter field, we generated synthetic rsfMRI time series at all $V = 32,492$ left cortical surface mesh vertices for $M = 1200$ time points with $t_r = 0.72s$, matching the HCP-YA protocol.

4.3. Implementation details

For the summary network $T_\psi(\cdot)$, we use a fully connected network with ReLU activations, with an initial non-trainable encoding layer which takes the Fourier transform of the BOLD signals y at the set of Nyquist frequencies. We set the number of hidden layers to be 3, with hidden widths $M, \lfloor \frac{M}{2} \rfloor, \lfloor \frac{M}{4} \rfloor$. For the marginal likelihood emulator $p_\gamma(\cdot|\cdot)$, we use a conditional neural spline normalizing flow (Durkan et al., 2019) with 5 spline coupling transforms, each with a fully connected 3 layer conditioning network with hidden widths of 64 and ReLU activations. Both networks are trained on synthetic data generated from the simulator outlined in Section 2 using Adam with a batch size of 100 and learning rate of 10^{-5} for 10^5 iterations. Note that separate summary network and likelihood model pairs were trained for the forward models (20) and (21).

For calibrating the simulator hyperparameters using the non-differentiable loss (19), we used Bayesian optimization (Frazier, 2018) under the expected improvement acquisition function for a total of 200 runs using the rsfMRI from a randomly selected HCP-YA subject and both forward models. The prior smoothness hyperparameters are selected by maximizing (17) over a pre-defined grid. For single subject analysis, this was repeated for each subject. For multi-subject analysis, we use a common set of smoothing parameters for all reconstructions, as is standard practice.

4.4. Competing Hemodynamic Estimators

For estimation under the one-parameter model (20), we compare our method against two alternative approaches. The first approach, referred to as *JointMAP*, performs vertex-wise joint MAP reconstruction under a standard l_1 sparsity prior on the signals

$$\left(\hat{\theta}_v, \hat{s}_v\right) = \min_{\theta \in \Theta, s \geq 0} \|y_v - A(\theta)s\|^2 + \eta \|s\|_1,$$

where $A(\theta) \in \mathbb{R}^{M \times M}$ is a convolution matrix formed from the kernel (20), $s \in \mathbb{R}^M$ denotes the discretized neural signals, and $\eta > 0$ is a regularization parameter. Optimization is performed using block-coordinate descent, where the (convex) subproblem in s is solved using alternating direction method of multipliers and the (non-convex) subproblem in θ is solved using golden section search. We set the penalty parameter $\eta = \sigma\sqrt{2 \log(M)}$, where σ is the calibrated noise level. The second approach, referred to as *DUP* (deep unrolled prior), adapts Gossard and Weiss (2024) to perform vertex-wise joint reconstruction. Specifically, DUP first pre-trains an unrolled network $\mathcal{A}_\rho : \mathbb{R}^M \times \mathbb{R}^{M \times M} \mapsto \mathbb{R}^M$, parameterized by weights ρ , to minimize

$$\hat{\rho} = \min_{\rho} \mathbb{E}_{p(\theta, s, y)} \|\mathcal{A}_\rho(y, A(\theta)) - s\|_2^2,$$

then estimates the hemodynamic parameters by minimizing the reconstructed error

$$\hat{\theta}_v = \min_{\theta \in \Theta} \|A(\theta)\mathcal{A}_{\hat{\rho}}(y_v, A(\theta)) - y_v\|_2^2, \quad (22)$$

via golden section search. We take \mathcal{A}_ρ to be a 5-layer unrolled fully connected ReLU network with hidden width M and train on synthetic data from the simulator model in Section 2 using Adam (learning rate 10^{-5} , 10^5 iterations, batch size 100). We also attempted to compare our method against Cherkaoui et al. (2021). However, extending their method to a high-resolution surface mesh proved computationally intractable, which is not surprising as the approach was originally developed to work on coarse, atlas-based surface discretizations.

For the two-parameter model (21), we compare our method to Wu et al. (2013), implemented in the MATLAB package *rsHRF* (Wu et al., 2021). *rsHRF* uses a two stage procedure, first estimating neural spike times by thresholding the fMRI time series, then estimating hemodynamic parameters conditional on the detected spikes. We used the suggested defaults for all method hyperparameters.

4.5. Evaluation

4.5.1. Hemodynamic Reconstruction

To evaluate the performance of the hemodynamic estimation on synthetic data, we compute the mean squared error (MSE) and bias of the reconstructions, averaged over the mesh. The quality of the uncertainty quantification procedure from Section 3.5 is assessed by the empirical coverage of the 95% pointwise intervals. In the synthetic data experiments, this is computed as the fraction of mesh locations for which the intervals cover the true hemodynamic parameter. For in-vivo data, where we lack access to ground truth, we instead approximate the empirical coverage of the intervals using the HCP test-retest data; where one scan is used to form the intervals and their empirical coverage is calculated over the reconstructions from the other scan. Because hemodynamic response shape is expected to be relatively stable within healthy subjects between multiple scans over a short time period (months), the test-retest scans can be (approximately) considered as independent replications from model (4) with the same θ , though different s and ϵ , and thus can be used to assess the stability of our hemodynamic coupling estimation methodology. We also compute the average interval length over the mesh for use as a scalar measure of reconstruction uncertainty.

4.5.2. Connectivity

Spatial variability in the cortical hemodynamic response can bias downstream functional connectivity estimates (Lindquist et al., 2009; Rangaprakash et al., 2018). We therefore evaluate whether our spatially varying hemodynamic estimates can improve connectivity analysis by comparing seed-based effective connectivity computed from three signal representations: I) raw (non-deconvolved) BOLD signals, II) deconvolved BOLD signals assuming a spatially constant and known hemodynamic response, III) deconvolved BOLD signals under a spatially varying hemodynamic response estimated by our methodology. Under the LTI forward model (3), with a known response kernel (either fixed or pre-estimated), the resulting linear inverse problem for latent signal reconstruction has been widely studied. For simplicity, we choose to perform deconvolution using the Wiener filter (Wiener, 1949), acknowledging that better performance may be obtained through more modern techniques. Using a predefined seed region of interest (ROI), we estimate the effective connectivity from the time series at each non-ROI vertex to the ROI-averaged time series. We use a bivariate Granger Causality (GC) based definition of effective connectivity (Roebroeck et al., 2005) with an autoregressive lag of 2. For each non-ROI vertex, p-values are calculated from the F -tests assessing GC and then corrected to control false discovery rate at the 0.05 level using the Benjamini-Hochberg procedure (Benjamini and Hochberg, 1995).

4.5.3. Population Analysis

We evaluate inter-subject variation of the hemodynamic field estimates using the functional principal components analysis (fPCA) approach proposed in (Lila et al., 2016). For a cohort of N subjects, fPCA is used to obtain the Karhunen–Loève decomposition of the scalar hemodynamic coupling parameter $\tilde{\theta}_i(x_v)$ for subject i at location x_v :

$$\tilde{\theta}_i(x_v) = \tilde{\mu}(x_v) + \sum_{k=1}^{N-1} z_{ik} \tilde{\varphi}_k(x_v), \quad (23)$$

where $\tilde{\mu}(x_v)$ is the mean function, $\tilde{\varphi}_k(x_v)$ are orthonormal eigenfunctions, and the scores z_{ik} are mean-zero, uncorrelated random variables with $\text{Var}(z_{ik}) = \lambda_k$. The eigenvalues λ_k are non-increasing in k . The first few eigenfunctions represent the dominant modes of spatial variation in the hemodynamic coupling parameter across subjects, while the corresponding scores quantify the contribution of each mode for an individual subject.

We use the scan-1 rsfMRI data from $N = 100$ unrelated HCP-YA subjects to compute $\tilde{\mu}$, $\{\tilde{\varphi}_k\}_{k=1}^{N-1}$ and the corresponding subject specific score $\{z_{ik}\}_{k=1, i=1}^{N-1, N}$. fPCA implies a reduced rank estimate of the covariance of $\tilde{\theta}$, which is given by

$$\text{Cov}_{\tilde{\theta}}(x_j, x_{j'}) \approx \sum_{k=1}^{N-1} \lambda_k \tilde{\varphi}_k(x_j) \tilde{\varphi}_k(x_{j'}), \quad j, j' \in 1, \dots, V. \quad (24)$$

This will be used to identify cortical regions with large inter-subject hemodynamic variability. The estimated scores will be used as covariates in a regression model for predicting simple subject-specific features to evaluate the use of the reconstructed hemodynamic fields as a biomarker.

Table 1: Synthetic-data results: estimation performance (MSE, bias) and uncertainty quantification (empirical coverage (EC) and average interval length), averaged across the cortical surface.

<i>(A) One-parameter model (20)</i>			<i>(B) Two-parameter model (21)</i>			
Method	MSE	Bias	θ_1		θ_2	
			MSE	Bias	MSE	Bias
JointMAP	0.4619	0.6281	0.2573	0.4755	0.7824	-0.6924
DUP	0.4867	0.6526				
MPM	0.0632	-0.0149				
Ours	0.0101	-0.0028	1.934×10^{-4}	0.0021	0.2284	0.0070

<i>(C) Uncertainty quantification</i>				
	Model (20)		Model (21)	
	θ_1	θ_1	θ_1	θ_2
EC	0.9168	0.9974	0.9737	
Interval Length	0.3852	0.07894	1.4204	

5. Results

5.1. Synthetic Data Results

Table 1 A) compares the estimation results for the synthetic data using the one-parameter model (20). Our method exhibits mean squared errors and biases that are, on average, an order of magnitude smaller than both JointMAP and DUP. Recall that both of the competitors perform joint reconstruction of signal and hemodynamic parameters, resulting in the estimation of the latter being dependent on the estimation of the former. Since even the non-blind signal reconstruction is ill-posed in this setting, we attribute the poorer performance of the competing methods, at least in part, to the propagation of errors from the signal reconstruction to the target hemodynamic estimation. Our approach avoids this issue by marginalizing the signal out of the data likelihood.

The second key differentiating feature of our method is the incorporation of spatial regularization. To evaluate its effect, we drop the prior from Section 3.2 and apply the learned marginal posterior mean (6), denoted MPM, independently to each mesh BOLD time series. As shown in the third row of Table 1 A), on average, this results in a greater than $6\times$ increase in the MSE compared to our spatially regularized framework. While MPM outperforms both JointMAP and DUP owing to its avoidance of explicit signal reconstruction, we see that incorporating spatial smoothness of the hemodynamics provides substantial additional improvement.

Table 1 B) shows the estimation results for the two-parameter forward model (21). Estimation of θ_1 echoes the results from Table 1 A), where our method again results in an order of magnitude reduction in average MSE compared to rsHRF. Although our method exhibits lower MSE for θ_2 as well, both approaches perform relatively poorly for this parameter.

Table 1 C) shows the 95% empirical pointwise coverage and average interval length for the procedure from Section 3.5 for both synthetic datasets. For the one-parameter model (20), we see reasonably good empirical coverage, with slight overconfidence. For the two-parameter model (21), the coverage on θ_1 indicates a bit of conservatism, though the

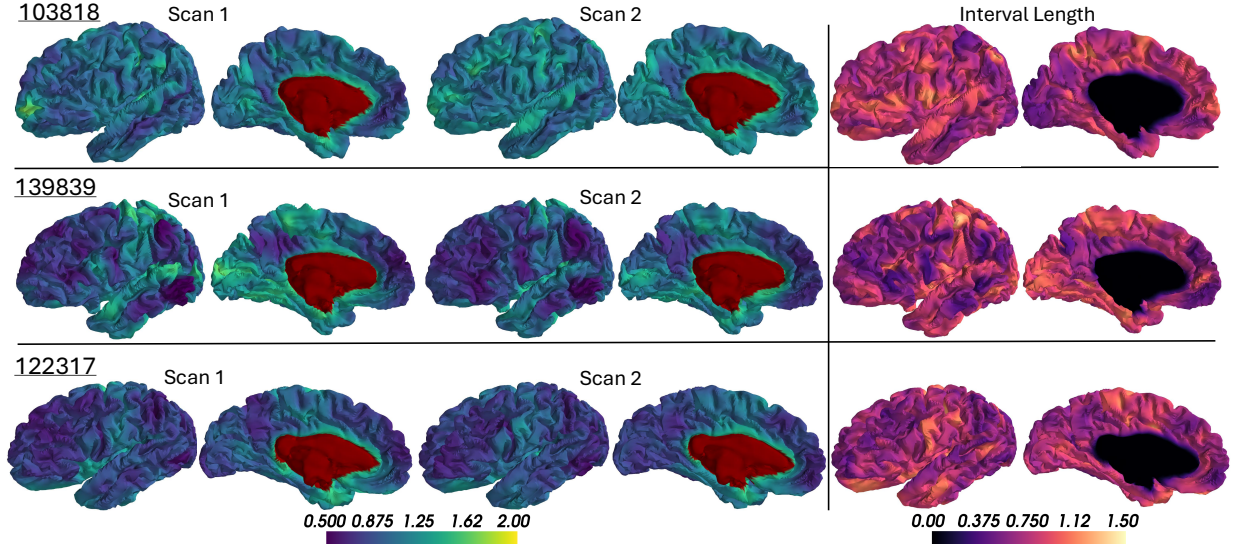


Figure 3: (Left) Estimates of the θ -field for the one-parameter hemodynamic coupling model (20) on the HCP test-retest data for three randomly selected subjects. Inter-subject variability is noticeably larger than within-subject between-scan variability. (Right) Length of the 95% pointwise intervals calculated from the procedure in Section 3.5 on the Scan 1 data.

intervals are quite tight, indicating strong statistical identifiability of this parameter. While the empirical coverage for θ_2 is reasonable, the estimation uncertainty is excessively large. Indeed, given $\theta_2 \in [-1, 1]$, the average interval length occupies approximately 70% of the possible values of the parameter. Coupled with the relatively poor estimation performance for both methods for θ_2 , these results imply there are likely fundamental limitations on its statistical identifiability in resting-state data under HCP-style acquisition and noise level.

5.2. In-vivo Data Results

In this section, we apply our methodology under the one-parameter model (20) to the real resting-state HCP data. We choose this model over model (21) due to the superior statistical identifiability of model parameters reported in Section 5.1.

5.2.1. Hemodynamic Reproducibility

The spatial maps of $\hat{\theta}$ for 3 randomly selected HCP test-retest subjects are shown in the left part of Figure 3. Qualitatively, we see that between-subject variability is noticeably larger than within-subject (between-scan) variability for each subject, with many unique subject-specific spatial features preserved across scans. This result is also apparent quantitatively, as the average within-subject squared norm of the difference between scan 1 and scan 2 (≈ 0.0214) was substantially lower than the average between-subject squared norm (≈ 0.0590).

For each subject in Figure 3, we ran the uncertainty quantification procedure from Section 3.5 on the scan 1 data to construct pointwise 95% intervals for the reconstructed field. The resulting interval lengths are shown in the right part of Figure 3. We notice substantial spatial variability in these maps, indicating the reconstruction uncertainty is highly location dependent. We evaluated the empirical coverage of these intervals on the

estimates from the scan 2 data. The average empirical coverage was $\approx 98.5\%$, indicating good calibration with mild conservatism.

5.2.2. Population Analysis

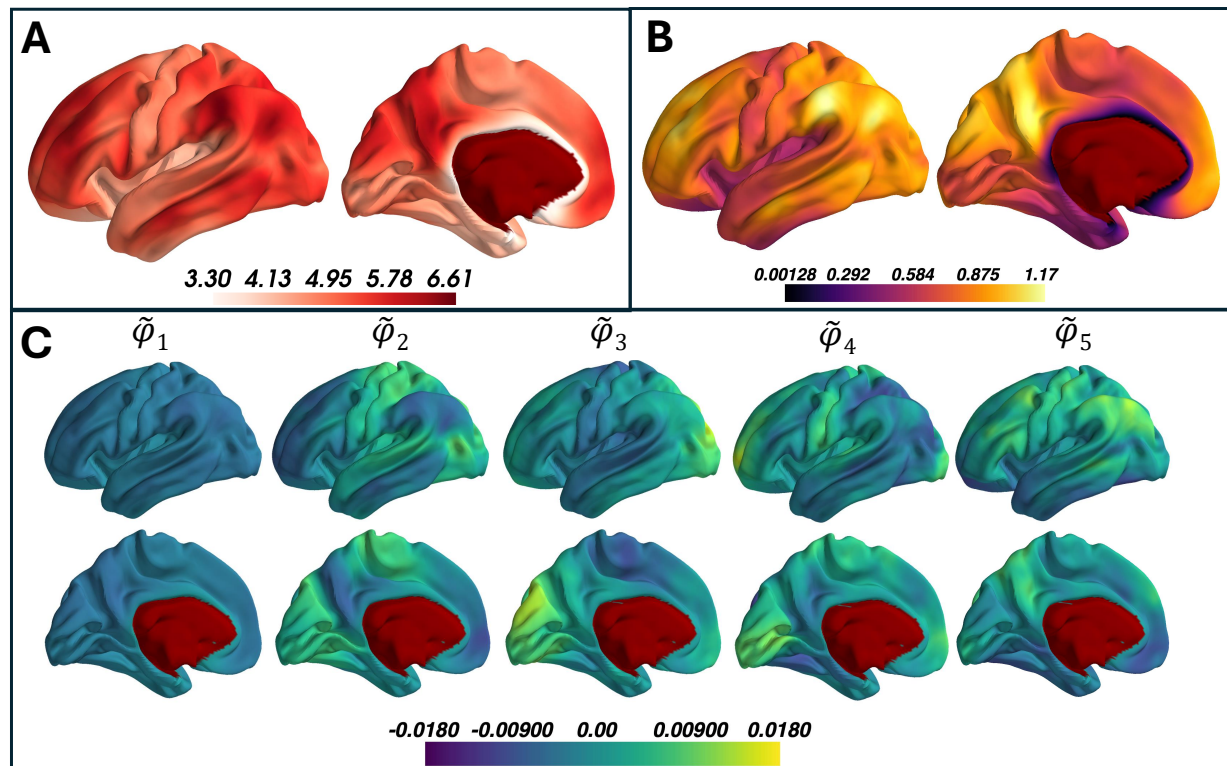


Figure 4: A) Time-to-peak (in seconds) of mean hemodynamic field, B) pointwise standard deviation of the hemodynamic field $\tilde{\theta}(x)$, C) and the first 5 eigenfunctions $\tilde{\varphi}_k$, describing the main modes of inter-subject variability, estimated from 100 unrelated HCP-YA subjects under the one-parameter model (20).

As displayed in Figure 2, large θ in model (20) implies less latency in the BOLD signal, that is, shorter *time-to-peak*, where time-to-peak is defined as $\operatorname{argmax}_t h_\theta(t)$. Panel A of Figure 4 shows the time-to-peak (in seconds) of the HRF evaluated at the estimated mean parameter field $\mu = g^{-1}(\tilde{\mu})$, across the cortical surface. We note less latency in several of the visual and motor areas (occipital and pre/postcentral gyrus), along with some regions in the inferior temporal lobe. Areas with more latency include regions in the frontal and inferior parietal lobes. Panel B of Figure 4 shows the point-wise standard deviation of the transformed parameter $\tilde{\theta}$, estimated using the low-rank approximation (24). We see large variances in areas of the frontal lobe and inferior parietal lobe, indicating substantial inter-subject variability. This is consistent with the subject-level results in Figure 3, where the frontal-lobe hemodynamics of the leftmost subject differ substantially from those of the other two subjects. These results highlight the well-documented inter-subject hemodynamic variability (Lindquist et al., 2009).

We investigate the utility of the hemodynamic field reconstructions as a potential imaging biomarker by regressing two outcomes recorded in the HCP-YA subjects, sex and number of times tobacco was used on the day of the scan, using the first five subject-specific

scores from the decomposition (23). These two outcomes were chosen as simple targets for a proof-of-concept evaluation, rather than to draw novel biological conclusions. For each outcome, we fit an independent logistic (sex) or linear (tobacco use) regression using the full sample of $N = 100$ subjects. For the sex outcome, the regression coefficient associated with $\tilde{\varphi}_5$ was significant. For tobacco use, the regression coefficient associated with $\tilde{\varphi}_2$ was significant. These associations can be interpreted in terms of the spatial pattern of variability in the corresponding eigenfunctions in panel C of Figure 4. Detailed biological interpretation of the implicated regions is beyond the scope of this work, our goal is simply to demonstrate the biomarker potential of θ .

5.2.3. Connectivity Analysis

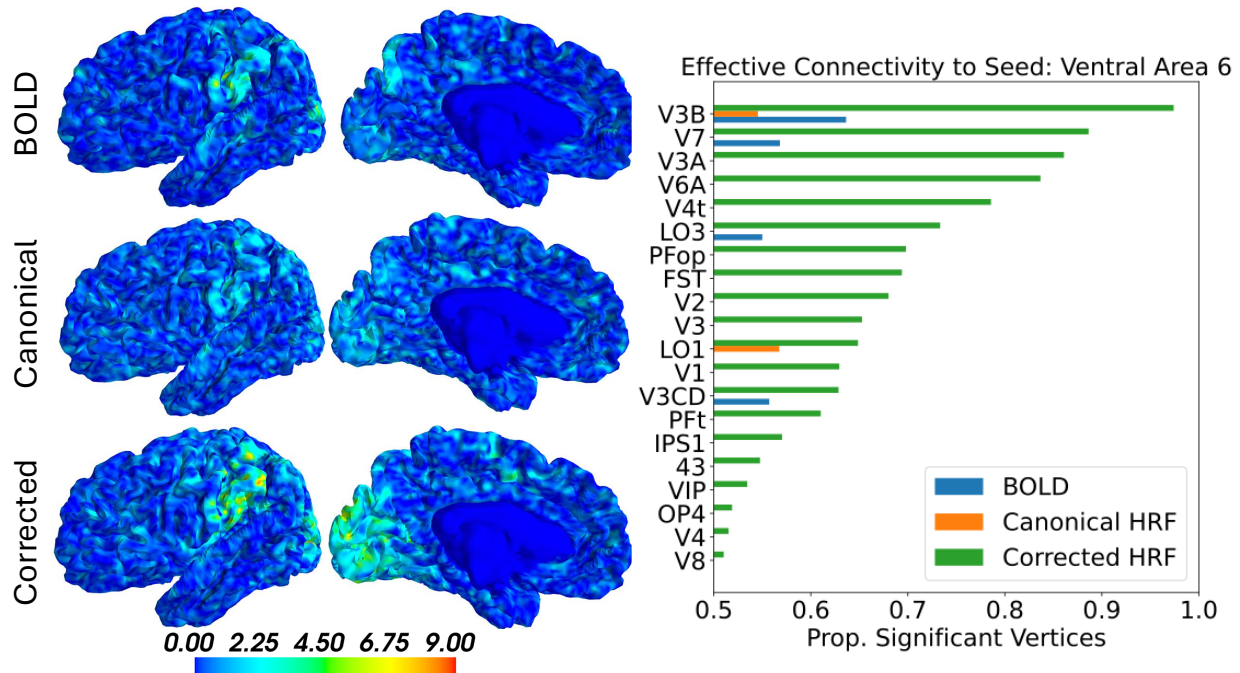


Figure 5: (Left) $-\log_{10}$ -transformed p-values for testing GC from each mesh vertex to average signal in Left Ventral Area 6. (Right) Regions in the Glasser atlas with at least 50% of vertices exhibiting significant GC to Left Ventral Area 6, for the three considered signal representations.

Using the procedure in Section 4.5.2, we compared the seed-based effective connectivity for raw BOLD (BOLD), deconvolution with a spatially fixed canonical response (Canonical, $\theta = 1$ in (20)), and deconvolution with our spatially varying hemodynamics (Corrected). We used scan-1 data from subject 103818 (hemodynamic field shown in Figure 3, left), with the seed ROI set to Left Ventral Area 6 (Glasser atlas) (Glasser et al., 2016). This ROI was chosen because it exhibited the largest average $\hat{\theta}$ (≈ 1.5), thus providing strong contrast with the spatially constant model.

Figure 5 (left) shows the spatial maps of the $-\log_{10}$ -transformed FDR corrected p-values from the GC tests. To interpret this spatial pattern, we calculated the proportion of mesh vertices in each parcel of the Glasser atlas where the GC was significant at the 0.05 level. Regions with $\geq 50\%$ of significant mesh vertices were deemed strongly effectively

connected, and are shown in the right panel of Figure 5. We see that all of the strongly connected regions identified by BOLD and Canonical are also detected by our deconvolved signals (Corrected). However, the effective connectivity estimated under our corrected HRF identifies many additional regions, primarily located within the dorsal visual stream, occipital lobe and parietal lobe. This pattern is highly consistent with the established functional connectivity of Left Ventral Area 6 reported in the literature (Baker et al., 2018).

6. Conclusion and Discussion

In this work, we present a new methodology for estimating a spatially varying, subject-specific forward model of hemodynamic coupling from resting-state fMRI. To disentangle estimation of the latent neural signal from that of the forward hemodynamic model, we adopt a marginal likelihood approach in which the latent signal is marginalized out. The resulting objective function is approximated using a deep conditional density estimator. Spatial regularization is enforced via a latent Gaussian process prior, and estimation uncertainty is quantified using a double-bootstrap procedure. Given the estimated forward model, latent neural signals can then be recovered using any standard non-blind inference method. In both synthetic and in-vivo datasets, our approach results in more accurate hemodynamic estimates and improves downstream connectivity analyses versus standard competing methods.

A thus far understated feature of our method is computational efficiency. By exploiting the sparsity of the prior precision over a finite element basis, estimation can be performed on ultra high resolution meshes using off-the-shelf algorithms to solve the sparse linear system (13). For instance, point estimation on the 32,492 vertex surface mesh took on average around 30 seconds for model (20) and about 150 seconds for model (21), on a personal CPU machine with 36GB of RAM and 12 cores. Note that while these runtimes already make this method practical for practitioners to run on standard modern laptops, it is highly likely they could be (significantly) improved by migrating the code to a GPU, which would speed both the backpropagation used to compute the derivatives in (14) and (15) as well as the preconditioned conjugate gradient solves by leveraging existing GPU-optimized implementations.

This work has a few limitations. While empirical results on both synthetic and in-vivo data indicate good calibration of the double bootstrap algorithm for uncertainty quantification, a limitation of this work is the computational burden of this procedure, as it requires BR point estimates. In practice, we use $B = 100$ and $R = 20$ and ran the code in sequence. However, each of the outer bootstraps is independent and therefore can be parallelized, provided sufficient computational resources. In our experiments, we use a pairwise measure of Granger causality to estimate effective connectivity, which is somewhat unsatisfactory since it also detects indirect interactions. This choice was made for computational feasibility, as full multivariate Granger causality measures tend to scale poorly with the dimension of the time series (order V^2) (Shojaie and Fox, 2022), making application to the full surface-based mesh time series of dimension $V = 32,492$ impractical.

Our method can be extended in several ways. There are a variety of hemodynamic forward models that have been proposed in the literature, each with their own level of

approximation fidelity to the true hemodynamic response. Failure to account for the misspecification due to this forward model discrepancy can result in varying degrees of bias, and so a principled manner of accommodating this within our learned marginal likelihood framework is of interest. In our experiments, we use a classical deconvolution to estimate the neural signals under the corrected hemodynamic forward model independently at each vertex. In reality, there exists a complex dependence structure in the neural signals, mediated by both local and non-local white matter fiber tracts. Designing a high-resolution signal inverter that is able to effectively leverage this correlation is of significant interest.

References

- Armijo, L. (1966). Minimization of functions having lipschitz continuous first partial derivatives. *Pacific Journal of mathematics* 16(1), 1–3.
- Bailes, S. M., D. E. Gomez, B. Setzer, and L. D. Lewis (2023, aug). Resting-state fmri signals contain spectral signatures of local hemodynamic response timing. *eLife* 12, e86453.
- Baker, C. M., J. D. Burks, R. G. Briggs, J. R. Sheets, A. K. Conner, C. A. Glenn, G. Sali, T. M. McCoy, J. D. Battiste, D. L. O’Donoghue, et al. (2018). A connectomic atlas of the human cerebrum—chapter 3: the motor, premotor, and sensory cortices. *Operative Neurosurgery* 15(suppl_1), S75–S121.
- Benjamini, Y. and Y. Hochberg (1995). Controlling the false discovery rate: a practical and powerful approach to multiple testing. *Journal of the Royal statistical society: series B (Methodological)* 57(1), 289–300.
- Buckner, R. L. (2003). The hemodynamic inverse problem: Making inferences about neural activity from measured mri signals. *Proceedings of the National Academy of Sciences* 100(5), 2177–2179.
- Buxton, R. B., E. C. Wong, and L. R. Frank (1998). Dynamics of blood flow and oxygenation changes during brain activation: the balloon model. *Magnetic resonance in medicine* 39(6), 855–864.
- Caballero-Gaudes, C., S. Moia, P. Panwar, P. A. Bandettini, and J. Gonzalez-Castillo (2019). A deconvolution algorithm for multi-echo functional mri: Multi-echo sparse paradigm free mapping. *NeuroImage* 202, 116081.
- Cao, X., B. Sandstede, and X. Luo (2019). A functional data method for causal dynamic network modeling of task-related fmri. *Frontiers in neuroscience* 13, 127.
- Chan, T. F. and C.-K. Wong (1998). Total variation blind deconvolution. *IEEE transactions on Image Processing* 7(3), 370–375.
- Cherkaoui, H., T. Moreau, A. Halimi, C. Leroy, and P. Ciuciu (2021). Multivariate semi-blind deconvolution of fmri time series. *NeuroImage* 241, 118418.

- Durkan, C., A. Bekasov, I. Murray, and G. Papamakarios (2019). Neural spline flows. *Advances in neural information processing systems* 32.
- Frazier, P. I. (2018). A tutorial on bayesian optimization. *arXiv preprint arXiv:1807.02811*.
- Glasser, M. F., T. S. Coalson, E. C. Robinson, C. D. Hacker, J. Harwell, E. Yacoub, K. Ugurbil, J. Andersson, C. F. Beckmann, M. Jenkinson, et al. (2016). A multi-modal parcellation of human cerebral cortex. *Nature* 536(7615), 171–178.
- Glasser, M. F., S. M. Smith, D. S. Marcus, J. L. Andersson, E. J. Auerbach, T. E. Behrens, T. S. Coalson, M. P. Harms, M. Jenkinson, S. Moeller, et al. (2016). The human connectome project’s neuroimaging approach. *Nature neuroscience* 19(9), 1175–1187.
- Glasser, M. F., S. N. Sotiropoulos, J. A. Wilson, T. S. Coalson, B. Fischl, J. L. Andersson, J. Xu, S. Jbabdi, M. Webster, J. R. Polimeni, et al. (2013). The minimal preprocessing pipelines for the human connectome project. *Neuroimage* 80, 105–124.
- Gossard, A. and P. Weiss (2024). Training adaptive reconstruction networks for blind inverse problems. *SIAM Journal on Imaging Sciences* 17(2), 1314–1346.
- Hall, P. and J. Horowitz (2013). A simple bootstrap method for constructing nonparametric confidence bands for functions. *The Annals of Statistics*, 1892–1921.
- Havlicek, M., K. J. Friston, J. Jan, M. Brazdil, and V. D. Calhoun (2011). Dynamic modeling of neuronal responses in fmri using cubature kalman filtering. *Neuroimage* 56(4), 2109–2128.
- Jiang, B., T.-y. Wu, C. Zheng, and W. H. Wong (2017). Learning summary statistic for approximate bayesian computation via deep neural network. *Statistica Sinica*, 1595–1618.
- Karahanoglu, F. I., C. Caballero-Gaudes, F. Lazeyras, and D. Van De Ville (2013). Total activation: fmri deconvolution through spatio-temporal regularization. *NeuroImage* 73, 121–134.
- Lai, M.-J. and L. L. Schumaker (2007). *Spline functions on triangulations*. Number 110. Cambridge University Press.
- Lange, N. and S. L. Zeger (2002, 01). Non-linear fourier time series analysis for human brain mapping by functional magnetic resonance imaging. *Journal of the Royal Statistical Society Series C: Applied Statistics* 46(1), 1–29.
- Lila, E., J. A. D. Aston, and L. M. Sangalli (2016). Smooth Principal Component Analysis over two-dimensional manifolds with an application to neuroimaging. *The Annals of Applied Statistics* 10(4), 1854 – 1879.
- Lindgren, F., H. Rue, and J. Lindström (2011). An explicit link between gaussian fields and gaussian markov random fields: the stochastic partial differential equation approach. *Journal of the Royal Statistical Society Series B: Statistical Methodology* 73(4), 423–498.

- Lindquist, M. A. (2008). The statistical analysis of fmri data.
- Lindquist, M. A., J. M. Loh, L. Y. Atlas, and T. D. Wager (2009). Modeling the hemodynamic response function in fmri: efficiency, bias and mis-modeling. *Neuroimage* 45(1), S187–S198.
- Loh, J. M., M. A. Lindquist, and T. D. Wager (2008). Residual analysis for detecting mis-modeling in fmri. *Statistica Sinica*, 1421–1448.
- Ogawa, S., D. W. Tank, R. Menon, J. M. Ellermann, S. G. Kim, H. Merkle, and K. Ugurbil (1992). Intrinsic signal changes accompanying sensory stimulation: functional brain mapping with magnetic resonance imaging. *Proceedings of the National Academy of Sciences* 89(13), 5951–5955.
- Politis, D. N. and J. P. Romano (1994). The stationary bootstrap. *Journal of the American Statistical association* 89(428), 1303–1313.
- Rangaprakash, D., R. L. Barry, and G. Deshpande (2023). The confound of hemodynamic response function variability in human resting-state functional mri studies. *Frontiers in Neuroscience* 17, 934138.
- Rangaprakash, D., R. Tadayonnejad, G. Deshpande, J. O’Neill, and J. D. Feusner (2021, Jun). Fmri hemodynamic response function (hrf) as a novel marker of brain function: applications for understanding obsessive-compulsive disorder pathology and treatment response. *Brain Imaging and Behavior* 15(3), 1622–1640.
- Rangaprakash, D., G.-R. Wu, D. Marinazzo, X. Hu, and G. Deshpande (2018). Hemodynamic response function (hrf) variability confounds resting-state fmri functional connectivity. *Magnetic Resonance in Medicine* 80(4), 1697–1713.
- Roebroeck, A., E. Formisano, and R. Goebel (2005). Mapping directed influence over the brain using granger causality and fmri. *Neuroimage* 25(1), 230–242.
- Salimi-Khorshidi, G., G. Douaud, C. F. Beckmann, M. F. Glasser, L. Griffanti, and S. M. Smith (2014). Automatic denoising of functional mri data: combining independent component analysis and hierarchical fusion of classifiers. *Neuroimage* 90, 449–468.
- Shojaie, A. and E. B. Fox (2022). Granger causality: A review and recent advances. *Annual Review of Statistics and Its Application* 9(1), 289–319.
- Singh, M. F., A. Wang, T. S. Braver, and S. Ching (2020). Scalable surrogate deconvolution for identification of partially-observable systems and brain modeling. *Journal of neural engineering* 17(4), 046025.
- Uruñuela, E., J. Gonzalez-Castillo, C. Zheng, P. Bandettini, and C. Caballero-Gaudes (2024). Whole-brain multivariate hemodynamic deconvolution for functional mri with stability selection. *Medical Image Analysis* 91, 103010.

- Wang, J., H. Zhu, J. Fan, K. Giovanello, and W. Lin (2013). Multiscale adaptive smoothing models for the hemodynamic response function in fmri. *The annals of applied statistics* 7(2), 904.
- Wiener, N. (1949, 08). *Extrapolation, Interpolation, and Smoothing of Stationary Time Series: With Engineering Applications*. The MIT Press.
- Wipf, D. and H. Zhang (2014). Revisiting bayesian blind deconvolution. *Journal of Machine Learning Research (JMLR)*.
- Wu, G.-R., N. Colenbier, S. Van Den Bossche, K. Clauw, A. Johri, M. Tandon, and D. Marinazzo (2021). rshrf: A toolbox for resting-state hrf estimation and deconvolution. *NeuroImage* 244, 118591.
- Wu, G.-R., W. Liao, S. Stramaglia, J.-R. Ding, H. Chen, and D. Marinazzo (2013). A blind deconvolution approach to recover effective connectivity brain networks from resting state fmri data. *Medical Image Analysis* 17(3), 365–374.
- Yan, W., L. Palaniyappan, P. F. Liddle, D. Rangaprakash, W. Wei, and G. Deshpande (2021, 12). Characterization of hemodynamic alterations in schizophrenia and bipolar disorder and their effect on resting-state fmri functional connectivity. *Schizophrenia Bulletin* 48(3), 695–711.
- Yan, W., D. Rangaprakash, and G. Deshpande (2018). Aberrant hemodynamic responses in autism: Implications for resting state fmri functional connectivity studies. *NeuroImage: Clinical* 19, 320–330.
- Zayane, C. and T. M. Laleg-Kirati (2015). A sensitivity analysis of fmri balloon model. *Computational and mathematical methods in medicine* 2015(1), 425475.
- Zhang, T., F. Li, L. Beckes, C. Brown, and J. A. Coan (2012). Nonparametric inference of the hemodynamic response using multi-subject fmri data. *NeuroImage* 63(3), 1754–1765.
- Zhang, T., F. Li, L. Beckes, and J. A. Coan (2013). A semi-parametric model of the hemodynamic response for multi-subject fmri data. *NeuroImage* 75, 136–145.